Cobalt Induced PdO Formation in Low-Loading Pd/BEA Catalysts for CH_4 Oxidation

Junjie Chen[1], Kevin Giewont[1], Eric A. Walker[2], Jungkuk Lee[1], Yubiao Niu[3], Eleni A. Kyriakidou[1,*]

[1] *Department of Chemical and Biological Engineering, University at Buffalo, The State University of New York, Buffalo, NY 14260, USA*
[2] *Institute for Computational and Data Sciences, University at Buffalo, The State University of New York, Buffalo, NY 14260, USA*
[3] *College of Engineering, Swansea University, Bay Campus, Swansea, SA1 8EN, UK*

[*] Corresponding author: elenikyr@buffalo.edu (E.A. Kyriakidou).

Abstract

Palladium (Pd)/zeolite-based catalysts have shown great promise in low-temperature CH_4 oxidation reactions. However, improving the low-temperature performance of Pd/zeolite catalysts while simultaneously decreasing Pd usage remains a challenge. Herein, we demonstrate that incorporation of cobalt (Co) into 0.5 wt.% Pd/BEA (Pd(0.5)/BEA) can substantially boost the CH_4 oxidation performance. Specifically, increasing Co loading from 0 to 1 wt.% led to a continuous improvement in the CH_4 oxidation activity, with T_{50} (temperature that 50% conversion is achieved) decreasing from >500 ^oC over Pd(0.5)/BEA to 352 ^oC over Pd(0.5)Co(1.0)/BEA. Moreover, the CH_4 oxidation reaction rate of Pd(0.5)Co(1.0)/BEA was 77% greater than that of Pd(1.0)/BEA. Experimental evidence from CH_4-TPR, H_2-TPR, O_2-TPD, HAADF-STEM, EDS, and apparent activation energy studies suggested that the promotion effect of Co incorporation is attributed to the formation of highly active PdO, instead of less active ionic Pd. Stability tests over Pd(0.5)Co(1.0)/BEA showed comparable CH_4 oxidation activity with Pd(1.0)/BEA and slightly improved H_2O resistance. Density functional theory calculations revealed that Co is more stable than Pd at the ion-exchange sites (Al sites) of BEA zeolite. Co being more stable than Pd at the ion-exchanged sites leads to less ion-exchange sites available for Pd, thus less ionic Pd but more PdO nanocluster formation over bimetallic PdCo/BEA catalysts.

Keywords: *Bimetallic, ionic Pd, PdO, CH_4 oxidation, DFT*

TOC

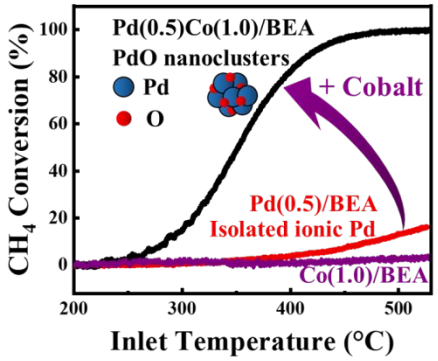

1. Introduction

The increasingly stringent emission standards introduced by the U.S. Environmental Protection Agency (EPA) force the transition from traditional fuels (gasoline, diesel) to cleaner ones, e.g. natural gas, hydrogen.[1] Natural gas (> 90% CH_4 content) is regarded as one of the most promising clean fuels because of the large number of natural gas reserves available in the US.[2] Natural gas is also more economically-friendly compared to other fossil fuels and it has high energy density (high H/C ratio). Natural gas is used as a fuel for compressed natural gas (CNG) vehicles, which have lower CO_2, CO, non-CH_4 hydrocarbon, and NO_x emissions compared to traditional diesel and gasoline vehicles. However, unburned CH_4 released from CNG vehicles raises a significant environmental concern due to its high global warming potential (GWP). Specifically, the GWP of CH_4 is about 25 times greater than that of CO_2 based on 100-years.[3] Thus, abatement of CH_4 emissions has become increasingly important.

Among different technologies used for CH_4 emission control, catalytic oxidation of CH_4 has attracted significant attention.[4-6] Nevertheless, catalytic oxidation of CH_4 at low temperatures (< 400 ^oC) remains a great challenge because CH_4 has four highly stable C-H bonds (bond energy of 413 kJ/mol).[7] Platinum group metal (PGM) (e.g., Pd, Pt, Rh) based catalysts have a higher CH_4 oxidation activity at low temperatures compared to transition metal or rare-earth based catalysts.[5] There are several studies available on the use of nonprecious metal catalysts for CH_4 oxidation, such as $Ni/Ce_xZr_{1-x}O_2$[8,9] and $NiCo_2O_4$[10]. However, the performance of nonprecious metal catalysts is lower than that of PGM based catalysts, while most of them require a high catalyst loading, low gas hour space velocity (GHSV) or high CH_4 feed concentrations. Thus, PGMs are still necessary

to satisfy the requirement of CH_4 emission control, that is low CH_4 concentrations (500-1500 ppm) and high GHSV. Among other PGMs, palladium (Pd) based catalysts have shown the most promising CH_4 oxidation performance.[6,11] Different Pd-based catalysts have been evaluated for their CH_4 oxidation performance, such as Pd@CeO_2,[12] Pd@ZrO_2,[13] Pd/Al_2O_3,[14] and Pd/zeolites (Pd/ZSM-5,[15,16] Pd/MOR,[17] Pd/SSZ-13[18]). Zeolites have attracted significant attention as they are endowed with high porosity, well-defined channels, and enhanced hydrothermal stability. Based on those unique properties, zeolites are able to confine well-dispersed metal nanoclusters and avoid metal sintering, which is challenging to achieve over traditional metal oxide supports (e.g. Al_2O_3, CeO_2, ZrO_2).[19,20] Therefore, Pd-based zeolite catalysts have shown an improved CH_4 oxidation performance compared to metal oxide supported catalysts. For example, Li et al. reported that the temperatures that 50-100% CH_4 conversion was achieved over Pd/ZSM-5 were 70-80 ^oC lower than the ones of Pd/Al_2O_3.[21] However, Pd price is prohibitive due its low reserves. Thus, decreasing Pd usage in Pd/zeolite catalysts is desired.

Pd species in zeolites can be present as either PdO nanoclusters or atomically dispersed ionic Pd,[22] with PdO nanoclusters believed to be more active than isolated ionic Pd towards the CH_4 oxidation reaction.[23,24] Recently, Khivantsev et al. showed that the state of Pd within the zeolite structure depends on the Pd loading.[25] In Pd/SSZ-13 (Si/Al = 6) with Pd loading lower than 2 wt.%, the majority of Pd was present in its ionic state. For Pd loadings greater than 2 wt.%, most of Pd aggregated to form PdO nanoclusters. Moreover, Gao et al. showed that the CH_4 oxidation turn-over rate decreased from 0.27 to 0.02 s^{-1} when the Pd loading of Pd/SSZ-13 (Si/Al = 6) decreased from 2 wt.% to 1 wt.%.[26] The decrease in CH_4 oxidation turn-over rate with decreasing Pd loading was attributed to the formation of more isolated Pd(II) cations that are less active than PdO nanoparticles form at higher Pd loadings. Therefore, decreasing the Pd loading in Pd/zeolite catalysts while maintaining the PdO active sites is challenging.

Incorporation of a second, non-precious, metal into Pd/zeolite catalysts was shown to improve the low-temperature CH_4 oxidation performance. Shi et al. incorporated a series of metals in Pd/HZSM-5, including Ce, Zr, Zn, Cu, Fe, Mn, Ca, Mg, and Li.[27,28] Among all studied catalysts, Pd-Zr/HZSM-5 and Pd-Ce/HZSM-5 were able to reach 100% CH_4 conversion at a lower temperature compared to Pd/HZSM-5 by 55 and 40 ^oC, respectively. Combined with CH_4-temperature programmed reduction (TPR) and O_2-temperature programmed desorption (TPD) experiments, Shi et al. reported that incorporation of Zr or Ce in Pd/HZSM-5 weakened the Pd-O

bond, resulting to an improved reactivity of surface oxygen species. More recently, Xie et al. reported that 2 wt.% Pd/NaLa-ZSM-5 achieved complete CH_4 oxidation at 320 ^oC, 60 ^oC lower compared to 2 wt.% Pd/Na-ZSM-5 under dry conditions.[29] The authors attributed this behavior to the improved Pd dispersion and the oxidation state of Pd^{2+} in PdO. Specifically, Pd^{2+} in PdO over 2 wt.% Pd/NaLa-ZSM-5 was more cationic that the one present in 2 wt.% Pd/Na-ZSM-5.

Even though the improvements made in the development of efficient Pd/zeolite catalysts for the CH_4 oxidation reaction, it is still challenging to improve their low-temperature performance while decreasing Pd usage. Herein, it is shown for the first time that incorporation of cobalt (Co) as a second metal in 0.5 wt.% Pd/BEA significantly improves the CH_4 oxidation performance compared to its monometallic counterpart. The CH_4 oxidation performance (under dry and wet feed conditions) of bimetallic PdCo/BEA and monometallic Pd/BEA was evaluated through light-off and stability tests. A combination of high angle annular dark field-scanning transmission electron microscopy (HAADF-STEM) images, energy dispersive X-ray spectroscopy (EDS) elemental maps, H_2-TPR, and O_2-TPD was applied to characterize the impact of Co incorporation on the distribution of PdO nanoclusters and ionic Pd species. CH_4 oxidation reaction rates and apparent activation energy measurements were conducted to investigate the intrinsic catalytic activity of monometallic Pd/BEA and bimetallic PdCo/BEA catalysts. Moreover, density functional theory (DFT) calculations were performed to optimize the local structure of Pd/BEA and Co/BEA. Finally, a mechanism for Co induced PdO nanocluster formation in PdCo/BEA catalysts was proposed.

2. Experimental

2.1. Catalyst synthesis

Protonic from BEA zeolite (HBEA) was prepared by calcining ammonium form BEA zeolites (CP814E, Zeolyst) with Si/Al = 12.5 at 500 ^oC for 2 h. Bimetallic PdCo/BEA was synthesized by incipient wetness impregnation. Briefly, for the synthesis of Pd(0.5 wt.%)Co(1.0 wt.%)/BEA, 0.475 mL of 0.1 M $Pd(NO_3)_2{\cdot}4NH_3$ solution (10 wt.% in H_2O, Sigma Aldrich) and 0.343 mL of 0.5 M $Co(NO_3)_2{\cdot}6H_2O$ (ACS, $\geq$ 98%, Sigma Aldrich) were pre-mixed and diluted with 0.632 mL D.I. water as the pore volume of HBEA is 1.45 ml/g. The mixed precursor solution was then added to 1 g of BEA zeolites and the slurry was mixed vigorously for 20 min. For comparison, 1 wt.% Co/BEA and 1 wt.% Pd/BEA were also prepared as described above.

Monometallic catalysts are denoted as M(x)/BEA, where M represents the active metal (Pd, Co) and x its weight loading (wt.%). Bimetallic catalysts are labeled as Pd(0.5)Co(y)/BEA, where y is the Co loading (wt.%). The synthesized catalysts are listed in Table 1. For comparison purposes, 1 wt.% Pd/γ-Al_2O_3 was synthesized by incipient wetness impregnation using γ-Al_2O_3 (Sasol, surface area: 142 m^2/g, pore volume: 0.463 cm^3/g) as the support and $Pd(NO_3)_2 \cdot 4NH_3$ (10 wt.% in H_2O, Sigma Aldrich) as the Pd precursor. All synthesized catalysts were dried at 110 ^oC for 8 h followed by calcination at 500 ^oC for 2 h (10 ^oC/min).

2.2. Characterizations

The textural properties (Brunauer-Emmett-Teller (BET) surface areas and Barrett-Joyner-Halenda (BJH) pore volumes) of HBEA support and as-prepared catalysts (Pd/BEA, Co/BEA, and PdCo/BEA) were measured with a Tri-Star II surface area and porosity analyzer (Micromeritics). Before each measurement, the samples were degassed at 150 ^oC for 3 h with a Micromeritics VacPrep 061. The desorption branch of the collected isotherms was used to calculate the BJH pore volumes.

X-ray diffraction (XRD) patterns of the studied samples were collected using a Rigaku Ultima IV instrument equipped with a Cu Kα X-ray source. The X-ray diffraction patterns were collected in a range of 2θ = 5-60º with a scan rate of 1.2º/min.

HAADF-STEM images and EDS elemental maps of the studied samples were obtained with a FEI Talos F200X Transmission Electron Microscope. The samples were dusted on Cu grids followed by a gentle purge with air to remove excess powder not attached to the grid.

CH_4-TPR-mass spectroscopy (CH_4-TPR-MS) experiments were conducted to study the initial reactivity of the oxygen species on the studied catalysts. The reactor setup for CH_4-TPR-MS experiments is described in section *2.3*. In general, 100 mg of catalyst (250-500 μm) was first pretreated at 500 ^oC for 30 min under 20% O_2/Ar to remove adsorbed impurities. The catalyst was then cooled down to room temperature under the same gas flow followed by introduction of 1500 ppm CH_4 balanced by Ar with a flow rate of 166.5 sccm (cm^3/min, STP). After the feed gas was balanced, the catalyst temperature was raised to 700 ^oC with a temperature ramp of 5 ^oC/min. CH_4 (m/z = 15), CO_2 (m/z = 44), H_2O (m/z = 18), CO (m/z = 29), and H_2 (m/z = 2) signals were continuously recorded by a mass spectrometer (Pfeiffer Omnistar GSD 320).

In situ CO diffuse reflectance infrared Fourier transform spectroscopy (DRIFTS) was performed using a Nicolet iS50 FTIR spectrometer (Thermo Fisher) equipped with a high temperature reaction chamber (Harrick Praying Mantis). In each test, about 20 mg of sample was loaded in the sample cell and pretreated under pure Ar (100 sccm) at 200 ^{o}C for 30 mins. After the pretreatment, the sample was cool down to room temperature and a background spectrum was collected. 1% CO/Ar (100 sccm) was then switched to the sample which was saturated for 30 mins following by purging with Ar for another 30 mins to remove gas phase CO. CO adsorption spectra were collected with a resolution of 4 cm^{-1} and 32 scans.

H_2-TPR was performed using a Micromeritics AutoChem II 2920 equipment with a thermal conductivity detector (TCD). 50 mg of catalyst was loaded in a U-shaped quartz reactor. The catalyst was first pretreated with 20% O_2/Ar at 500 ^{o}C (50 sccm) for 30 mins and purged with Ar for another 30 mins to remove gas phase O_2. The catalyst was then cooled down to -20 ^{o}C under Ar before 50 sccm of 10% H_2/Ar was introduced in the reactor. After the TCD signal was stabilized, the catalyst was heated up to 1000 ^{o}C (10 ^{o}C /min).

O_2-TPD was conducted in the same reactor setup as described in section *2.3*. Specifically, 50 mg of spent catalyst (250-500 μm) was first pretreated with 20% O_2/Ar at 500 ^{o}C for 30 min. The catalyst was then cooled down to 200 ^{o}C and purged with Ar for 1 h before heating up to 850 ^{o}C with a ramp rate of 20 ^{o}C/min under 50 sccm Ar. Oxygen (m/z = 32) desorption profiles were recorded by a mass spectrometer.

2.3. Catalytic performance evaluations

The CH_4 oxidation performance of the as-synthesized catalysts was evaluated in a home-built packed bed reactor equipped with an online MKS FTIR gas analyzer (MultiGas 2030).[30,31] 100 mg of catalyst (250-500 μm) was loaded in a U-shaped quartz tube reactor (I.D. = 8 mm) and was stabilized between two small plugs of quartz wool. Before the catalytic evaluation, the catalysts were pretreated at 550 ^{o}C for 1 h under the reaction feed (1500 ppm CH_4, 5% O_2, balanced with Ar). The flow rate was 166.5 sccm, which corresponds to a weight based hourly space velocity (WHSV) of 99,900 $mL g_{cat}^{-1} h^{-1}$. The CH_4 oxidation performance under wet conditions (5% H_2O) was also evaluated. H_2O steam was generated in a tube furnace set to 200 ^{o}C and was carried to the reactor by Ar. H_2O was introduced in the tube furnace by a syringe pump (D-series pump (Teledyne Isco)). CH_4 conversions (X) were calculated using Eq. (1).

$$CH_4 \text{ conversion:} \qquad X = \frac{(C_{CH_4,in} - C_{CH_4,out})}{C_{CH_4,in}} \times 100\% \qquad (1)$$

Where $C_{CH_4,\,in}$ and $C_{CH_4,\,out}$ represent the CH_4 concentration in the inlet and outlet of the reactor.

The CH_4 oxidation reaction rates of Pd(0.5)Co(x)/BEA (x=0, 0.5) and Pd(1.0)/BEA catalysts were measured by performing steady state experiments where the reaction feed (1500 ppm CH_4, 5% O_2, Ar balanced, WHSV = 99,900 $mL g_{cat}^{-1} h^{-1}$) remained constant while the catalyst reaction temperature was varied. Before reaction rate measurements the catalysts were pretreated under the reaction feed at 550 °C for 1 h. In all cases, CH_4 conversion was kept < 15% to minimize the impact of heat and mass transfer effects. The catalyst was kept at each reaction temperature for at least 30 min. The apparent activation energies (E_{app}) of Pd(0.5)Co(x)/BEA (x=0, 0.5) and Pd(1.0)/BEA catalysts were calculated from the Arrhenius plot. CH_4 oxidation reaction rates (r) were calculated using Eq. (2)

$$\text{Reaction rate: } r\left(\mu mol_{CH_4} \mu mol_{Pd}^{-1} s^{-1}\right) = \frac{C_{CH_4,in}\left(166.5 \times \frac{10^{-3} L}{60\ s}\right)}{22.4 \frac{L}{mol} \times 0.1 g_{cat} \times \frac{M_{Pd}}{106.4 g/mol}} \times X \qquad (2)$$

Where M_{Pd} represents the Pd loading.

The stability and water resistance of Pd(0.5)Co(x)/BEA (x=0, 0.5) and Pd(1.0)/BEA were tested by keeping the catalyst temperature at 450 °C while varying the feed gas composition. Specifically, the catalysts were first pretreated in a similar manner as the CH_4 oxidation reaction rate measurements and their catalytic performance was initially evaluated under dry conditions (1500 ppm CH_4, 5% O_2, Ar balanced, 99,900 $mL g_{cat}^{-1} h^{-1}$) for 10 h. Then, 5% H_2O was introduced in the reactor for 5 h to evaluate the hydrothermal stability of the studied catalysts. Finally, water was removed from the reactor feed and the recoverability of the studied catalysts was evaluated over a 25 h period.

2.4. Computational Methods

All theoretical work conducted in this study performs periodic Kohn-Sham density functional theory (DFT) calculations using the Vienna Ab initio Simulation Package (VASP).[32,33] Plane wave pseudopotentials were used to treat the wavefunctions and the projector augmented-wave method was used to treat core electrons.[34] Two functionals were used to optimize geometries and calculate the ground state energies: the Perdew−Burke−Ernzerhof (PBE) functional[35,36] and the Bayesian error estimation functional with van der Waals correction (BEEF-vdw).[37]

A blank BEA unit cell was acquired from the database of zeolite structures.[38] From the blank framework, dual aluminum placements were enumerated throughout one of the 12-membered ring channels in a single unit cell (total of 70 different combinations). The Dual aluminum placements models were considered because each one is compensated by an ion, Pd or Co. During aluminum enumeration, two background electrons were added to account for the negative charge of each aluminum since they were uncompensated (no charge compensating metal or hydrogen) and monopole and dipole corrections were applied.[39] Energies of uncompensated structures are taken relative to the lowest energy structure which is referenced as 0 eV. Calculations concerning the 70 different aluminum combinations were performed using only the BEEF-vdw functional. The lowest energy aluminum placement was then used as a foundation to create Pd/BEA and Co/BEA structures. To create Pd/BEA and Co/BEA structures, Pd and Co were introduced near each aluminum site and then the geometry was optimized. Gaseous O_2 was introduced to the metal site (Pd or Co) and the geometry was once again optimized. Ground state energies of a Pd (111) slab, Co (0001) slab, gaseous O_2, and the metal slabs with one surface atom removed were also calculated to obtain the relative energy of the final zeolite structures. Eq. 3 shown below was used to find the relative energy of Pd/BEA and Co/BEA structures.

$$E_{rel} = E_{M/BEA} + 2E_{M\ slab^{-1}} - E_{BEA} - 2E_{M\ slab} \quad (3)$$

Where *E* represents the DFT calculated ground state energy of the respective subscript (excluding E_{rel}). *M/BEA* represents the final zeolite structures (Pd/BEA or Co/BEA), *BEA* represents the zeolite structure with two aluminums, *M slab* represents the respective metal slab, and *M slab*$^{-1}$ represents the respective metal slab with one surface atom removed. All calculations for Pd and Co structures are performed using both the BEEF-vdw and PBE functionals.

3. Results and discussions

3.1. BET and BJH

The N_2 adsorption and desorption isotherms of the studied samples are shown in Fig. S1. All samples showed a type I isotherm,[40] indicating that no significant textural changes were observed upon Pd and Co loading. The sharp N_2 adsorption and desorption at relative pressures <0.05 are attributed to the presence of micropores in the zeolite structure. The hysteresis loop at relative pressures > 0.7 is due to voids between BEA nanoparticles.

As shown in Table 1, incorporation of Pd and Co in BEA zeolites led to a decrease in the BEA surface area and BJH pore volume. For example, the surface area of Pd(0.5)/BEA (483 m^2/g) and Pd(0.5)Co(1.0)/BEA (488 m^2/g) decreased by 9% compared to the surface area of HBEA support (536 m^2/g). The surface area of monometallic Co(1.0)/BEA (428 m^2/g) and Pd(1.0)/BEA (432 m^2/g) decreased even further (by ~20%) compared to the surface area of HBEA, which can be related to the partial pore blockage due to metal incorporation.[41]

3.2. CH_4 oxidation performance

Fig.1a shows the CH_4 conversion as a function of temperature of monometallic Pd(x)/BEA (x = 0.5, 1), Co(1.0)/BEA, and bimetallic Pd(0.5)Co(x)/BEA (x = 0.1, 0.28, 0.5, 1.0, 1.5) catalysts. Monometallic Pd(1.0)/BEA outperformed all evaluated catalysts, with T_{50} and T_{90} equal to 331 and 392 °C, respectively. However, monometallic Pd(0.5)/BEA was able to achieve only 13% CH_4 conversion at 500 °C. The significant difference in CH_4 oxidation performance between Pd(1.0)/BEA and Pd(0.5)/BEA is attributed to the increased number of Pd^{2+} present in Pd(0.5)/BEA.[26] Incorporation of 0.1 wt.% Co in Pd(0.5)/BEA (Pd(0.5)Co(0.1)/BEA) resulted in an increase in CH_4 conversion from 13% (Pd(0.5)/BEA) to 70% (Pd(0.5)Co(0.1)/BEA) at 500 °C. Increasing the Co amount even further from 0.1 to 1 wt.%, led to a continuous decrease in T_{50}'s from 456 to 352 °C (Fig.1b). Interestingly, Pd(0.5)Co(1.0)/BEA showed a comparable CH_4 oxidation performance to monometallic Pd(1.0)/BEA. Increasing the Co loading to 1.5 wt.% did not further improve the catalytic performance. Specifically, the T_{50} and T_{90} of Pd(0.5)Co(1.5)/BEA were 8 and 10 °C higher than that of Pd(0.5)Co(1.0)/BEA. Thus, 1 wt.% Co is considered to be the optimal loading for the studied catalysts. Monometallic Co(1.0)/BEA was also evaluated towards CH_4 oxidation. Co(1.0)/BEA showed a negligible CH_4 oxidation performance with only 2.7% CH_4 conversion observed at 500 °C. This result indicates that the promotion effect of Co incorporation in Pd(0.5)/BEA is not attributed to the catalytic activity of Co itself. The performance of Pd(0.5)Co(1.0)/BEA was compared to literature reported Pd/BEA catalysts.[42-44] The T_{90} (420 °C) of Pd(0.5)Co(1.0)/BEA is much lower than that of 2.5 wt.% Pd/BEA (~450 °C) reported by Park et al.[42] Moreover, Pd(0.5)Co(1.0)/BEA had a comparable performance with 0.92 wt.% Pd/BEA reported by Friberg et al.,[43] even though a decreased amount of Pd(0.5)Co(1.0)/BEA (100 mg) was used for the catalyst evaluation compared to 0.92 wt.% Pd/BEA (~285 mg). However, the CH_4 oxidation light-off tests over Pd/BEA catalysts reported

in literature were conducted under different conditions than the ones reported in the attached manuscript (e.g. feed gas (CH_4, H_2O) concentrations, space velocity, etc.). Thus, a direct comparison of the catalyst performance is not possible. The state-of-the-art catalyst for CH_4 oxidation is Pd/Al_2O_3. Therefore, 1 wt.% Pd/γ-Al_2O_3 was also evaluated for comparison. Pd(1.0)/γ-Al_2O_3 had a comparable T_{50} with Pd(1.0)/BEA, but it reached a higher T_{90} (445 ^oC) than Pd(1.0)/BEA (392 ^oC) and Pd(0.5)Co(1.0)/BEA (420 ^oC) (Fig. S2 (a)).

CH_4 oxidation light-off curves in the presence of 5% H_2O are shown in Fig. S2 (b). The CH_4 oxidation performance of the studied catalysts was inhibited in the presence of H_2O. The detailed H_2O inhibition mechanism is discussed in *Section 3.7*. The CH_4 oxidation performance under wet conditions decreases in the following order: Pd(1.0)/BEA > Pd(1.0)/Al_2O_3 > Pd(0.5)Co(1.0)/BEA >> Pd(0.5)/BEA. Increasing the Pd loading from 0.5 wt.% (Pd(0.5)/BEA) to 1 wt.% (Pd(1.0)/BEA) and incorporating Co in Pd(0.5)/BEA (Pd(0.5)Co(1.0)/BEA) promoted the CH_4 conversion under wet conditions from 3% (Pd(0.5)/BEA) to 92% (Pd(1.0)/BEA) and 80% (Pd(0.5)Co(1.0)/BEA) at 500 ^oC.

3.3. CH_4 temperature programmed reduction

CH_4-TPR experiments were further applied to characterize the reactivity of Pd species towards gaseous CH_4 in the absence of gas-phase O_2. The CH_4-TPR profiles, including CH_4 consumption, CO_2, H_2O, CO, and H_2 formation, are shown in Fig. 2. As shown in Fig. 2 (a-c), monometallic Pd(1.0)/BEA and bimetallic Pd(0.5)Co(1.0)/BEA showed similar CH_4 consumption profiles starting from 175-200 ^oC. However, monometallic Pd(0.5)/BEA showed negligible CH_4 conversion at temperatures <500 ^oC. This observation is consistent with the CH_4 oxidation light-off curves (Fig. 1a), where Pd(1.0)/BEA and Pd(0.5)Co(1.0)/BEA showed a comparable CH_4 oxidation performance, while Pd(0.5)/BEA showed much lower activity in the studied temperature range (<12%). Formation of CO_2 and H_2O was also observed starting at ~175 ^oC over Pd(1.0)/BEA and Pd(0.5)Co(1.0)/BEA (H_2O desorption at 100-170 ^oC is attributed to desorption of absorbed moisture instead of H_2O produced from the CH_4 oxidation reaction). Cobalt oxides have a very low CH_4 oxidation activity from 175 to 200 ^oC, evident by the CH_4 light-off test (Fig. 1) and CH_4-TPR profiles (Fig. 2d) over Co(1.0)/BEA. Thus, the first step during CH_4-TPR was attributed to the complete combustion of CH_4 over PdO, where gas-phase CH_4 reacts with bulk oxygen from PdO leading to CO_2 and H_2O formation.

CO and H_2 formation over Pd(1.0)/BEA and Pd(0.5)Co(1.0)/BEA was observed at around 275 ^oC (Figs. 2a, 2b), which can be attributed to CH_4 reforming reactions taking place including: dry reforming ($CH_4 + CO_2 \rightarrow 2CO + 2H_2$) and steam reforming ($CH_4 + H_2O \rightarrow CO + 3H_2$).[43] Metallic Pd is reported to be highly active for CH_4 steam/dry reforming reactions.[45] Thus, it can be hypothesized that part of PdO was reduced by CH_4 to form metallic Pd, which can serve as the active site for CH_4 reforming reactions. The CO_2 and H_2O signals over Pd(0.5)Co(1.0)/BEA and Pd(1.0)/BEA decreased to their baseline intensity when the temperature reached 425-450 ^oC, while the CO and H_2 signals kept increasing. This indicates that CH_4 reforming reactions prevail at this temperature range (425-450 ^oC) as the majority of PdO was reduced by CH_4.

Unlike Pd(1.0)/BEA and Pd(0.5)Co(1.0)/BEA catalysts, Pd(0.5)/BEA showed a different behavior during CH_4-TPR experiments (Fig. 2c). A negligible amount of CH_4 was consumed over Pd(0.5)/BEA at temperatures <540 ^oC, attributed to the decreased amount of PdO present in Pd(0.5)/BEA. A small CO_2 formation peak at ~300 ^oC can be attributed to PdO nanoclusters within this sample. At temperatures >500 ^oC, a small amount of CH_4 was consumed and complete oxidation products (CO_2, H_2O) were formed over Pd(0.5)/BEA, which can be associated with the reaction between ionic Pd and gas phase CH_4. Ionic Pd requires much higher temperatures to react with gas phase CH_4 compared to PdO as a result of its lower reactivity towards the CH_4 oxidation reaction.[26] CH_4 consumption increased sharply at 540 ^oC and CO, H_2 were simultaneously formed. This phenomenon can be attributed to reforming reactions taking place over metallic Pd, which was formed by the reduction of ionic Pd. Overall, CH_4-TPR experiments suggest that Co incorporation changed the state of Pd species from less active ionic Pd in Pd(0.5)/BEA to highly active PdO nanoclusters in Pd(0.5)Co(1.0)/BEA.

3.4. XRD, HAADF-STEM images, and EDS elemental maps

The XRD patterns of HBEA support, Co(1.0)/BEA, Pd(0.5)Co(x)/BEA (x = 0, 1.0), and Pd(1.0)/BEA catalysts are shown in Fig. S3. No peaks for Co_3O_4 (33.3º), CoO (36.3º), and PdO (33.9º) were observed, demonstrating that large cobalt oxides (Co_3O_4, CoO) and PdO nanoparticles were not present in the as-synthesized catalysts.

Considering the limited sensitivity of XRD, HAADF-STEM images and EDS elemental (Pd, Co) maps of Pd(0.5)Co(x)/BEA (x=0, 1.0), Pd(1.0)/BEA, and Co(1.0)/BEA catalysts were collected (Fig. 3). A small number of PdO nanoparticles are observed over Pd(0.5)/BEA (Fig. 3

(a.1, 2)) while the majority of Pd signal is attributed to well dispersed ionic Pd. This observation was also verified by HRTEM images (Fig. S4), where only a few PdO particles were observed. Moreover, CO-DRIFTS, H_2-TPR, and O_2-TPD were conducted to confirm that ionic Pd is the dominating Pd species in Pd(0.5)/BEA (discussed later). Increasing the Pd loading from 0.5 to 1 wt.% resulted to the formation of PdO nanoclusters over Pd(1.0)/BEA (Fig. 3 (c.1, 2)). Incorporation of 1 wt.% Co into Pd(0.5)/BEA lead to the formation of more PdO nanoclusters (Fig. 3 (b.1, 2)) compare to monometallic Pd(0.5)/BEA. This observation suggests that the Co induces the formation of PdO nanoclusters, which is desirable for the CH_4 oxidation reaction. Additional HRTEM images and PdO particle size distributions of Pd(1.0)/BEA and Pd(0.5)Co(1.0)/BEA catalysts are shown in Fig. S5. The average PdO particle size of Pd(1.0)/BEA and Pd(0.5)Co(1.0)/BEA were 2.2 and 2.3 nm, respectively. Co is well dispersed over the BEA zeolite in both Pd(0.5)Co(1.0)/BEA and Co(1.0)/BEA samples (Fig. 3(b.3), 4(d.2)). Moreover, no cobalt oxides nanoclusters were observed over Co(1.0)/BEA (Fig. S6), which is consistent with the XRD results (Fig. S3).

3.5. CO DRIFTS, H_2-TPR, and O_2-TPD

The ionic Pd species over Pd(0.5)Co(x)/BEA (x = 0, 1.0), Pd(1.0)/BEA were characterized by CO DRIFTS. As shown in Fig. 4a, both Pd(1.0)/BEA and Pd(0.5)/BEA contain multiple ionic Pd species. The peaks at 2152, 2134 cm^{-1} are attributed to Pd^{2+}-CO, peaks at 2117, 2096 cm^{-1} are attributed to Pd^{+}-CO, and the peak at 2078 cm^{-1} is associate to isolated Pd^{0}-CO.[46] The peaks at 2152, 2134, 2117 cm^{-1} over Pd(0.5)Co(1.0)/BEA disappeared after Co incorporation, suggesting that Co suppresses the ionic Pd species formation. A weak peak at 2096 cm^{-1} was observed over Pd(0.5)Co(1.0)/BEA, indicating that a small amount of Pd^{+} is present. No peaks were observed over Co(1.0)/BEA.

Bulk techniques, including H_2-TPR, and O_2-TPD, were applied to verify the cobalt induced PdO formation over bimetallic Pd(0.5)Co(1.0)/BEA. H_2-TPR profiles of Pd(0.5)Co(x)/BEA (x = 0, 1.0), Pd(1.0)/BEA, and Co(1.0)/BEA catalysts are shown in Fig. 4b. The low temperature desorption peaks between -8 to 0 ^{o}C present in every sample are associated with the desorption of Ar from the BEA framework.[47] No distinguishable peaks for Co(1.0)/BEA reduction were observed in the temperature range of 0-200 ^{o}C. A broad peak at 59.6 ^{o}C over Pd(0.5)/BEA can be attributed to the reduction of ionic Pd.[48] Moreover, no peaks were observed from 0-20 ^{o}C over

Pd(0.5)/BEA, suggesting a negligible PdO amount present. This observation is in agreement with the TEM images, EDS mapping (Fig. 3(a.1-2), Fig. S4) of Pd(0.5)/BEA. Increasing the Pd loading from 0.5 to 1.0 wt.% led to more PdO formation, evident by the new peak at 13.6 ^{o}C and the STEM image shown previously (Fig. 3(c.1)). Other than PdO, ionic Pd is also present in Pd(1.0)/BEA catalyst, as indicated by the presence of a reduction peak at 56 ^{o}C. The shoulder peak centered at ~18 ^{o}C can be attributed to overlapping of PdH_x decomposition and Pd^{2+} reduction. When 1.0 wt.% Co was introduced in Pd(0.5)/BEA, the reduction peak for ionic Pd disappeared and a new peak at 17.3 ^{o}C appeared, assigned to the reduction of PdO. This phenomenon is consistent with the improved CH_4 oxidation performance of Pd(0.5)Co(1.0)/BEA compared to monometallic Pd(0.5)/BEA catalyst.

O_2-TPD data of Pd(0.5)Co(x)/BEA (x = 0, 1.0), Pd(1.0)/BEA, and Co(1.0)/BEA catalysts is displayed in Fig. 4c. No O_2 desorption peak was observed over Pd(0.5)/BEA, suggesting that only a negligible amount of PdO is present in this sample. On the contrary, when the Pd loading increased from 0.5 to 1.0 wt.%, an O_2 desorption peak centered at 737 ^{o}C was observed, indicating PdO nanocluster formation. This observation is consistent with STEM images and EDS mapping in Fig. 3(c.1, 2) as well as the improved CH_4 oxidation performance of Pd(1.0)/BEA over Pd(0.5)/BEA. Incorporation of 1 wt.% Co along with 0.5 wt.% Pd in BEA zeolites led to an O_2 desorption peak centered at 772 ^{o}C, attributed to PdO decomposition as O_2 desorption was not observed over Co/BEA.

3.6. Apparent activation energies

The reaction rate and apparent activation energies of Pd(0.5)/BEA, Pd(0.5)Co(1.0)/BEA, and Pd(1.0)/BEA catalysts were measured to further verify the effect of Co. Fig. 5 shows that Pd(0.5)/BEA requires higher reaction temperatures (> 450 ^{o}C) to reach comparable CH_4 oxidation reaction rates to Pd(1.0)/BEA. Incorporation of 1 wt.% Co in Pd(0.5)/BEA improved the low temperature reaction rate significantly. The CH_4 oxidation reaction rate over Pd(0.5)Co(1.0)/BEA at 250 ^{o}C was 0.94×10^{-3} $\mu mol_{CH_4} \mu mol_{Pd}^{-1} s^{-1}$, which is 77% higher than that of the Pd(1.0)/BEA catalyst. The E_{app} of Pd(0.5)Co(1.0)/BEA and Pd(1.0)/BEA are similar to the E_{app} of previously reported PdO based catalysts,[17] suggesting that the dominating active species over these two samples are PdO nanoclusters. However, Pd(0.5)/BEA showed lower reaction rates and apparent activation energies compared to Pd(0.5)Co(1.0)/BEA and Pd(1.0)/BEA. The CH_4 oxidation

activity of Pd(0.5)/BEA can be attributed to the presence of a small amount of PdO (Fig. 3a1, a2), considering that ionic Pd is much less active in the CH_4 oxidation reaction.[26] In this work, the apparent activation energies of Pd(0.5)/BEA and Pd(0.5)Co(1.0)/BEA were measured at different temperature ranges (230-300 ^oC for Pd(0.5)Co(1.0)/BEA, 460-520 ^oC for Pd(0.5)/BEA) to obtain similar CH_4 oxidation rates. Based on Ribeiro et al.,[49] the apparent activation energy of CH_4 oxidation over PdO decreased from 125 to 30 kJ/mol with the increase in the reaction temperature as H_2O inhibition is less severe at high temperatures. Therefore, the low Eapp (46.3 kJ/mol) of Pd(0.5)/BEA can be attributed to a decrease in the H_2O inhibition effect at 460-520 ^oC. This observation is consistent with the CH_4 oxidation light-off tests, CH_4-TPR, and O_2-TPD results, suggesting that Co introduction in Pd(0.5)/BEA increased the amount of PdO and suppressed the formation of ionic Pd resulting to improved CH_4 oxidation performance compared to monometallic Pd(0.5)/BEA.

3.7. CH_4 oxidation stability tests

Stability tests of Pd(0.5)/BEA, Pd(0.5)Co(1.0)/BEA, and Pd(1.0)/BEA catalysts are shown in Fig. 6. For monometallic Pd(0.5)/BEA, the initial CH_4 conversion at 450 ^oC under the dry feed (1500 ppm CH_4, 5% O_2, 0% H_2O, Ar balance) is only about 1%, which is much lower than that of Pd(0.5)Co(1.0)/BEA (92%) and Pd(1.0)/BEA (98%) catalysts. Within the first 10 h under the dry feed, the CH_4 conversion of monometallic Pd(0.5)/BEA increased from 1 to 4%, which can be attributed to the formation of PdO from Pd^{2+} during the CH_4 oxidation reaction. The CH_4 conversion of Pd(0.5)Co(1.0)/BEA slightly increased, from 92 to 95%, in the first 3 h under the dry feed and it was maintained constant for 7 h, showcasing its high durability. Monometallic Pd(1.0)/BEA slightly deactivated in the first 10 h under the dry condition, with CH_4 conversion decreasing by 2%. In the second stage of the stability test, 5% H_2O was introduced in the reaction feed mixture while the catalyst temperature was maintained at 450 ^oC. All studied catalysts were significantly deactivated. Specifically, monometallic Pd(0.5)/BEA was fully deactivated after 5% H_2O was introduced. Two inhibition stages over monometallic Pd(1.0)/BEA and bimetallic Pd(0.5)Co(1.0)/BEA were observed. A rapid decrease in CH_4 conversion was observed over both catalysts when 5% H_2O was introduced in the reactor. This behavior is attributed to the competitive adsorption of H_2O and CH_4 on PdO.[50,51] A slow deactivation was observed after the initial rapid deactivation that is associated with the accumulation of OH groups on the zeolite

(close to PdO) and PdO surface.[52] Bimetallic Pd(0.5)Co(1.0)/BEA outperformed monometallic Pd(1.0)/BEA under the wet conditions, indicating that Co incorporation is also beneficial for the hydrothermal stability of the catalyst. In the last stage of the stability test, H_2O was removed from the reactor feed (at 15 h) to investigate the recoverability of the studied catalysts. Two recoverability stages were observed. The catalyst activity increased right after H_2O was removed, attributed to the quick desorption of H_2O from PdO due to the decrease of H_2O partial pressure. A slower second stage can be observed over all studied catalysts. The slow performance recovery is attributed to the transformation of less active $Pd(OH)_2$ to active PdO species.[53] The CH_4 conversion of monometallic Pd(0.5)/BEA increased to 3%, 25 h after H_2O was removed from the reactor feed, and was much lower than bimetallic Pd(0.5)Co(1.0)/BEA (X_{CH_4} = 85%) and monometallic Pd(1.0)/BEA (X_{CH_4} = 88%) catalysts. Overall, bimetallic Pd(0.5)Co(1.0)/BEA showed a similar CH_4 oxidation performance with Pd(1.0)/BEA catalyst during the stability test even though Pd(0.5)Co(1.0)/BEA contained half the amount of PGM compared to Pd(1.0)/BEA.

3.8. DFT computational results

A blank BEA unit cell was acquired from the database of zeolite structures.[38] From the blank framework, dual aluminum placements were enumerated throughout one of the 12-membered ring channels in a unit cell (total of 70 different combinations). Relative energies of 70 different dual aluminum placements calculated from the BEEF-vdw functional are shown in Fig. 7(a). With the increase of the number of T-sites between two aluminums from 1 to 6, the relative energies decreased from ~1.5 to 0 eV. Therefore, a BEA structure with 6 T-sites between two aluminum was proposed as the most stable configuration (Fig. S7). After that two Co or Pd atoms were added to the Al sites of the most stable BEA structure, and the final structures of Co/BEA and Pd/BEA are shown in Fig. 7(b, c). The relative energies of Co/BEA and Pd/BEA calculated from PBE and BEEF-vdw functionals are shown in Table 3. Both PBE and BEEF-vdw functionals showed that the BEA zeolite structure is more stable (lower in energy) when Co is associated with the aluminum site. PBE estimates a much larger difference (Co/BEA = -2.02 eV, Pd/BEA = 0.26 eV) between the energies of Co/BEA and Pd/BEA while BEEF-vdw predicts a much smaller difference (Co/BEA = -0.88 eV, Pd/BEA = -0.58 eV). These results imply that when Pd and Co are both present in the BEA zeolite structure, Co will attach to Al sites (ion exchange sites) of

BEA zeolite stronger than Pd. Therefore, less Al sites will be available for ionic Pd. And finally, more PdO nanocluster can be formed over the bimetallic PdCo/BEA catalyst.

4. Conclusions

In summary, this work introduces a facile method to improve the CH_4 oxidation performance of Pd/BEA catalyst and decrease Pd usage by incorporating Co as a second metal. Increasing Co loading from 0 to 1.0 wt.% in Pd(0.5)/BEA resulted to an improvement of the CH_4 oxidation performance compared to its monometallic counterpart. However, when Co loading was increased to 1.5 wt.%, the catalytic performance started declining. The CH_4 oxidation reaction rate over Pd(0.5)Co(1.0)/BEA was 77% higher than that of Pd(1.0)/BEA catalyst at 250 ^oC, suggesting that Co incorporation promotes the more efficient Pd usage. HAADF-STEM images, EDS elemental maps, H_2-TPR, and O_2-TPD results showed that Co incorporation in Pd/BEA catalysts led to PdO formation, which is more active compared to ionic Pd towards CH_4 oxidation. This phenomenon was also verified by apparent activation energies measurements, as bimetallic Pd(0.5)Co(1.0)/BEA showed similar E_{app} (~88.4 kJ/mol) with Pd(1.0)/BEA (~ 81.1 kJ/mol). DFT calculations predicted that Co is more stable than Pd at the ion-exchange sites (Al sites) of BEA zeolite, suggesting that less ion-exchanged sites are available for Pd resulting to more PdO nanocluster formation.

Acknowledgments:

This article was developed based upon funding from the Alliance for Sustainable Energy, LLC, Managing and Operating Contractor for the National Renewable Energy Laboratory for the U.S. Department of Energy. High performance computing utilized in this work was provided by the Center for Computational Research at University at Buffalo, the State University of New York. The authors would also like to acknowledge Dr. Richard E. Palmer and Dr. Cameron Pleydell-Pearce for the access to STEM and EDS facilities at Swansea University.

Supporting information. Nitrogen adsorption-desorption isotherms; CH_4 oxidation light-off tests under dry and wet conditions; XRD, HRTEM, PdO particle size distribution; the lowest energy dual aluminum structure (Fig. S1−S7). This material is available free of charge via the

Internet at https://nam12.safelinks.protection.outlook.com/?url=http%3A%2F%2Fpubs.acs.org%2F&data=04%7C01%7Celenikyr%40buffalo.edu%7C9d1e0f26bdda411fb82408d97f9d58c1%7C96464a8af8ed40b199e25f6b50a20250%7C0%7C0%7C637681136041946471%7CUnknown%7CTWFpbGZsb3d8eyJWIjoiMC4wLjAwMDAiLCJQIjoiV2luMzIiLCJBTiI6Ik1haWwiLCJXVCI6Mn0%3D%7C1000&sdata=4UGdpIEMXunlBTa59dF8axJ26i%2BcaoEZu5OM1OLgcTw%3D&reserved=0.

References:

1. U.S. Environmental Protection Agency (EPA). *U.S. Environmental Protection Agency (EPA).* Available online: https://www.epa.gov/emission-standards-reference-guide/all-epa-emission-standards (accessed 22 October 2020).
2. Powell, J. B., Natural gas utilization: Current status and opportunities. *Catal. Today* **2020,** 356, 27-36.
3. Solomon, S.; Manning, M.; Marquis, M.; Qin, D., *Climate change 2007-the physical science basis: Working group I contribution to the fourth assessment report of the IPCC*. Cambridge university press: 2007; Vol. 4.
4. Monai, M.; Montini, T.; Gorte, R. J.; Fornasiero, P., Catalytic Oxidation of Methane: Pd and Beyond. *Eur. J. Inorg. Chem.* **2018,** 2018, 2884-2893.
5. Gélin, P.; Primet, M., Complete oxidation of methane at low temperature over noble metal based catalysts: a review. *Appl. Catal., B* **2002,** 39, 1-37.
6. Jiang, D.; Khivantsev, K.; Wang, Y., Low-Temperature Methane Oxidation for Efficient Emission Control in Natural Gas Vehicles: Pd and Beyond. *ACS Catal.* **2020,** 10, 14304-14314.
7. Tang, P.; Zhu, Q.; Wu, Z.; Ma, D., Methane activation: the past and future. *Energy Environ. Sci.* **2014,** 7, 2580-2591.
8. Chen, J.; Carlson, B. D.; Toops, T. J.; Li, Z.; Lance, M. J.; Karakalos, S. G.; Choi, J. S.; Kyriakidou, E. A., Methane Combustion Over Ni/$Ce_xZr_{1-x}O_2$ Catalysts: Impact of Ceria/Zirconia Ratio. *ChemCatChem* **2020,** 12, 5558-5568.
9. Chen, J.; Buchanan, T.; Walker, E. A.; Toops, T. J.; Li, Z.; Kunal, P.; Kyriakidou, E. A., Mechanistic Understanding of Methane Combustion over Ni/CeO_2: A Combined Experimental and Theoretical Approach. ACS Catal. **2021**, 11, 9345-9354.
10. Tao, F. F.; Shan, J.; Nguyen, L.; Wang, Z.; Zhang, S.; Zhang, L.; Wu, Z.; Huang, W.; Zeng, S.; Hu, P., Understanding complete oxidation of methane on spinel oxides at a molecular level. *Nat. Commun.* **2015,** 6, 7798.
11. Lampert, J. K.; Kazi, M. S.; Farrauto, R. J., Palladium catalyst performance for methane emissions abatement from lean burn natural gas vehicles. *Appl. Catal., B* **1997,** 14, 211-223.
12. Cargnello, M.; Jaén, J. D.; Garrido, J. H.; Bakhmutsky, K.; Montini, T.; Gámez, J. C.; Gorte, R.; Fornasiero, P., Exceptional activity for methane combustion over modular Pd@CeO_2 subunits on functionalized Al_2O_3. *Science* **2012,** 337, 713-717.
13. Chen, C.; Yeh, Y.-H.; Cargnello, M.; Murray, C. B.; Fornasiero, P.; Gorte, R. J., Methane oxidation on Pd@ZrO_2/Si–Al_2O_3 is enhanced by surface reduction of ZrO_2. *ACS Catal.* **2014,** 4, 3902-3909.

14. Hurtado, P.; Ordóñez, S.; Sastre, H.; Dıez, F. V., Development of a kinetic model for the oxidation of methane over Pd/Al_2O_3 at dry and wet conditions. *Appl. Catal., B* **2004,** 51, 229-238.
15. Hosseiniamoli, H.; Bryant, G.; Kennedy, E. M.; Mathisen, K.; Nicholson, D.; Sankar, G.; Setiawan, A.; Stockenhuber, M., Understanding Structure–Function Relationships in Zeolite-Supported Pd Catalysts for Oxidation of Ventilation Air Methane. *ACS Catal.* **2018,** 8, 5852-5863.
16. de Correa, C. M.; Ai, H., Combustion of methane over palladium ZSM-5 and mordenite catalysts. *Appl. Catal., B* **1996,** 10, 313-323.
17. Petrov, A. W.; Ferri, D.; Krumeich, F.; Nachtegaal, M.; Van Bokhoven, J. A.; Kröcher, O., Stable complete methane oxidation over palladium based zeolite catalysts. *Nat. Commun.* **2018,** 9.
18. Lim, J. B.; Jo, D.; Hong, S. B., Palladium-exchanged small-pore zeolites with different cage systems as methane combustion catalysts. *Appl. Catal., B* **2017,** 219, 155-162.
19. Wang, N.; Sun, Q.; Bai, R.; Li, X.; Guo, G.; Yu, J., In situ confinement of ultrasmall Pd clusters within nanosized silicalite-1 zeolite for highly efficient catalysis of hydrogen generation. *J. Am. Chem. Soc.* **2016,** 138, 7484-7487.
20. Gu, J.; Zhang, Z.; Hu, P.; Ding, L.; Xue, N.; Peng, L.; Guo, X.; Lin, M.; Ding, W., Platinum nanoparticles encapsulated in MFI zeolite crystals by a two-step dry gel conversion method as a highly selective hydrogenation catalyst. *ACS Catal.* **2015,** 5, 6893-6901.
21. Li, Y.; Armor, J. N., Catalytic combustion of methane over palladium exchanged zeolites. *Appl. Catal., B* **1994,** 3, 275-282.
22. Lee, J.; Ryou, Y.; Cho, S. J.; Lee, H.; Kim, C. H.; Kim, D. H., Investigation of the active sites and optimum Pd/Al of Pd/ZSM–5 passive NO adsorbers for the cold-start application: Evidence of isolated-Pd species obtained after a high-temperature thermal treatment. *Appl. Catal., B* **2018,** 226, 71-82.
23. Wang, W.; Zhou, W.; Li, W.; Xiong, X.; Wang, Y.; Cheng, K.; Kang, J.; Zhang, Q.; Wang, Y., In-situ confinement of ultrasmall palladium nanoparticles in silicalite-1 for methane combustion with excellent activity and hydrothermal stability. *Appl. Catal., B* **2020,** 276, 119142.
24. Friberg, I.; Wang, A.; Olsson, L., Hydrothermal Aging of Pd/LTA Monolithic Catalyst for Complete CH_4 Oxidation. *Catalysts* **2020,** 10, 517.
25. Khivantsev, K.; Jaegers, N. R.; Kovarik, L.; Hanson, J. C.; Tao, F.; Tang, Y.; Zhang, X.; Koleva, I. Z.; Aleksandrov, H. A.; Vayssilov, G. N., Achieving Atomic Dispersion of Highly Loaded Transition Metals in Small-pore Zeolite SSZ-13: A New Class of High-capacity and High-efficiency Low Temperature CO and NOx Adsorbers. *Angew. Chem.* **2018**, 57, 16672-16677.
26. Cui, Y.; Zhu Chen, J.; Peng, B.; Kovarik, L.; Devaraj, A.; Li, Z.; Ma, T.; Wang, Y.; Szanyi, J.; Miller, J. T., Onset of High Methane Combustion Rates over Supported Palladium Catalysts: From Isolated Pd Cations to PdO Nanoparticles. *JACS Au* **2021,** 1, 396-408.
27. Shi, C.; Yang, L.; Cai, J., Cerium promoted Pd/HZSM-5 catalyst for methane combustion. *Fuel* **2007,** 86, 106-112.
28. Shi, C.-K.; Yang, L.-F.; Wang, Z.-C.; He, X.-E.; Cai, J.-X.; Li, G.; Wang, X.-S., Promotion effects of ZrO_2 on the Pd/HZSM-5 catalyst for low-temperature catalytic combustion of methane. *Appl. Catal., A* **2003,** 243, 379-388.
29. Xie, Y.; Zhang, L.; Jiang, Y.; Han, S.; Wang, L.; Meng, X.; Xiao, F.-S., Enhanced catalytic performance of methane combustion over zeolite-supported Pd catalysts with the lanthanum. *Catal. Today* **2021,** 364, 16-20.
30. Liu, C.-H.; Chen, J.; Toops, T. J.; Choi, J.-S.; Thomas, C.; Lance, M. J.; Kyriakidou, E. A., Hydrothermally Stable Pd/SiO2@Zr Core@Shell Catalysts for Diesel Oxidation Applications. Chem. Eng. J. 2021, 425, 130637.
31. Chen, J.; Rohani, P.; Karakalos, S. G.; Lance, M. J.; Toops, T. J.; Swihart, M. T.; Kyriakidou, E. A., Boron-hyperdoped silicon for the selective oxidative dehydrogenation of propane to propylene. *Chem. Commun.* **2020,** 56, 9882-9885.

32. Kresse, G.; Hafner, J., Ab initio molecular dynamics for liquid metals. *Phys. Rev. B* **1993,** 47, 558.
33. Kresse, G.; Furthmüller, J., Efficiency of ab-initio total energy calculations for metals and semiconductors using a plane-wave basis set. *Comput. Mater. Sci.* **1996,** 6, 15-50.
34. Blöchl, P. E., Projector augmented-wave method. *Phys. Rev. B* **1994,** 50, 17953.
35. Perdew, J. P.; Yue, W., Accurate and simple density functional for the electronic exchange energy: Generalized gradient approximation. *Phys. Rev. B* **1986,** 33, 8800.
36. Perdew, J. P.; Wang, Y., Accurate and simple analytic representation of the electron-gas correlation energy. *Phys. Rev. B* **1992,** 45, 13244.
37. Wellendorff, J.; Lundgaard, K. T.; Møgelhøj, A.; Petzold, V.; Landis, D. D.; Nørskov, J. K.; Bligaard, T.; Jacobsen, K. W., Density functionals for surface science: Exchange-correlation model development with Bayesian error estimation. *Phys. Rev. B* **2012,** 85, 235149.
38. C. Baerlocher, L. B. M., Database of Zeolite Structures, (n.d.). http://www.iza-structure.org/databases/ (accessed June 9, 2020).
39. Li, S.; Li, H.; Gounder, R.; Debellis, A.; Müller, I. B.; Prasad, S.; Moini, A.; Schneider, W. F., First-principles comparison of proton and divalent copper cation exchange energy landscapes in SSZ-13 zeolite. *J. Phys. Chem. C* **2018,** 122, 23564-23573.
40. Huang, Z.; Su, J.-F.; Guo, Y.-H.; Su, X.-Q.; Teng, L.-J., Synthesis of well-crystallized zeolite beta at large scale and its incorporation into polysulfone matrix for gas separation. *Chem. Eng. Commun.* **2009,** 196, 969-986.
41. Negoi, A.; Triantafyllidis, K.; Parvulescu, V. I.; Coman, S. M., The hydrolytic hydrogenation of cellulose to sorbitol over M (Ru, Ir, Pd, Rh)-BEA-zeolite catalysts. *Catal. Today* **2014,** 223, 122-128.
42. Park, J.-H.; Kim, B.; Shin, C.-H.; Seo, G.; Kim, S. H.; Hong, S. B., Methane Combustion over Pd Catalysts Loaded on Medium and Large Pore Zeolites. *Top. Catal.* **2008,** 52, 27-34.
43. Friberg, I.; Sadokhina, N.; Olsson, L., The effect of Si/Al ratio of zeolite supported Pd for complete CH_4 oxidation in the presence of water vapor and SO_2. *Appl. Catal., B* **2019,** 250, 117-131.
44. Friberg, I.; Clark, A. H.; Ho, P. H.; Sadokhina, N.; Smales, G. J.; Woo, J.; Auvray, X.; Ferri, D.; Nachtegaal, M.; Kröcher, O., Olsson, L., Structure and performance of zeolite supported Pd for complete methane oxidation. *Catal. Today* **2020**, https://doi.org/10.1016/j.cattod.2020.11.026
45. Masai, M.; Kado, H.; Miyake, A.; Nishiyama, S.; Tsuruya, S. Methane reforming by carbon dioxide and steam over supported palladium, platinum, and rhodium catalysts. *Stud. Surf. Sci. Catal.*, **1988**, 36, 67-71.
46. Zheng, Y.; Kovarik, L.; Engelhard, M. H.; Wang, Y.; Wang, Y.; Gao, F.; Szanyi, J., Low-Temperature Pd/Zeolite Passive NOx Adsorbers: Structure, Performance, and Adsorption Chemistry. *J. Phys. Chem. C* **2017,** 121, 15793-15803.
47. Adelman, B. J.; Sachtler, W. M. H., The effect of zeolitic protons on NOx reduction over Pd/ZSM-5 catalysts. *Appl. Catal., B* **1997,** 14, 1-11.48.
48. Ryou, Y.; Lee, J.; Kim, Y.; Hwang, S.; Lee, H.; Kim, C. H.; Kim, D. H., Effect of reduction treatments (H_2 vs. CO) on the NO adsorption ability and the physicochemical properties of Pd/SSZ-13 passive NOx adsorber for cold start application. *Appl. Catal., A* **2019,** 569, 28-34.
49. Zhu, G.; Han, J.; Zemlyanov, D. Y.; Ribeiro, F. H., Temperature dependence of the kinetics for the complete oxidation of methane on palladium and palladium oxide. *J. Phys. Chem. B* **2005,** 109, 2331-2337.
50. Ciuparu, D.; Lyubovsky, M. R.; Altman, E.; Pfefferle, L. D.; Datye, A. Catalytic Combustion of Methane over Palladium-based Catalysts. Catal. Rev.: Sci. Eng. **2002**, 44 (4), 593–649.
51. Gholami, R.; Alyani, M.; Smith, K. J., Deactivation of Pd Catalysts by Water during Low Temperature Methane Oxidation Relevant to Natural Gas Vehicle Converters. *Catalysts* **2015,** 5, 561-594.
52. Losch, P.; Huang, W.; Vozniuk, O.; Goodman, E. D.; Schmidt, W.; Cargnello, M., Modular Pd/zeolite composites demonstrating the key role of support hydrophobic/hydrophilic character in methane catalytic combustion. *ACS Catal.* **2019,** 9, 4742-4753.

53. Khivantsev, K.; Jaegers, N. R.; Kovarik, L.; Wang, M.; Hu, J. Z.; Wang, Y.; Derewinski, M. A.; Szanyi, J., The superior hydrothermal stability of Pd/SSZ-39 in low temperature passive NOx adsorption (PNA) and methane combustion. *Appl. Catal., B* **2021,** 280, 119449.

Cobalt Induced PdO formation in Low-Loading Pd/BEA Catalysts for CH_4 Oxidation

Table 1. BET surface areas and BJH pore volumes of HBEA, Pd(0.5)Co(x)/BEA (x = 0, 0.1, 0.28, 0.5, 1.0, 1.5), Co(1.0)/BEA, and Pd(1.0)/BEA catalysts, as well as their $T_{50,90}$'s for CH_4 oxidation (1500 ppm CH_4, 5% O_2, balanced by Ar, GHSV = 99,900 $mL g_{cat}^{-1} h^{-1}$).

Table 2. Apparent activation energies of Pd(0.5)Co(x)/BEA (x = 0, 1.0), and Pd(1.0)/BEA catalysts.

Table 3. Relative energies of Co/BEA and Pd/BEA using both the PBE and BEEF-vdw functionals.

Fig. 1. (a) CH_4 oxidation light-off curves, and (b) $T_{50,90}$ of CH_4 oxidation over Pd(0.5)Co(x)/BEA (x = 0, 0.1, 0.28, 0.5, 1.0, 1.5), Co(1.0)/BEA, and Pd(1.0)/BEA catalysts.

Fig. 2. CH_4-TPR over (a) Pd(1.0)/BEA, (b) Pd(0.5)Co(1.0)/BEA, and (c) Pd(0.5)/BEA catalysts (1500 ppm CH_4, balanced by Ar (GHSV = 99,900 $mL g_{cat}^{-1} h^{-1}$)).

Fig. 3. HAADF-STEM images and EDS elemental (Pd, Co) maps of fresh (a.1, 2) Pd(0.5)/BEA, (b.1-3) Pd(0.5)Co(0.1)/BEA, (c.1, 2) Pd(0.5)Co(1.0)/BEA, and (d.1, 2) Co(1.0)/BEA catalysts.

Fig. 4. (a) CO DRIFTS (b) H_2-TPR over fresh Pd(0.5)Co(x)/BEA (x = 0, 1.0), Pd(1.0)/BEA, and Co(1.0)/BEA catalysts, (c) O_2-TPD of used Pd(0.5)Co(x)/BEA (x = 0, 1.0), Pd(1.0)/BEA, and Co(1.0)/BEA catalysts.

Fig. 5. Arrhenius plot and apparent activation energies for CH_4 oxidation over Pd(0.5)Co(x)/BEA (x = 0, 1.0) and Pd(1.0)/BEA catalysts.

Fig. 6. Stability tests of CH_4 oxidation over Pd(0.5)Co(x)/BEA (x = 0, 1.0), and Pd(1.0)/BEA catalysts under dry (1500 ppm CH_4, 5% O_2, balanced by Ar) and wet (1500 ppm CH_4, 5% O_2, 5% H_2O, balanced by Ar) conditions, GHSV = 99,900 $mL g_{cat}^{-1} h^{-1}$.

Fig. 7. (a) Relative energies of 70 different dual aluminum placements within a 12-membered ring channel in a single BEA unit cell calculated using the BEEF-vdw functional (Energies are taken relative to the lowest energy structure; Neighbor away refers to the number of T-sites between both aluminums). Final structures of (b) Co/BEA and (c) Pd/BEA. Geometries shown here are optimized using the BEEF-vdw functional.

Table 1. BET surface areas and BJH pore volumes of HBEA, Pd(0.5)Co(x)/BEA (x = 0, 0.1, 0.28, 0.5, 1.0, 1.5), Co(1.0)/BEA, and Pd(1.0)/BEA catalysts, as well as their $T_{50,90}$'s for CH_4 oxidation (1500 ppm CH_4, 5% O_2, balanced by Ar, GHSV = 99,900 $mL g_{cat}^{-1} h^{-1}$).

Sample	Surface area (m^2/g)	Pore volume (cm^3/g)	T_{50} (°C)	T_{90} (°C)
HBEA	536	0.795	n.a.	n.a.
Pd(0.5)/BEA	483	0.783	> 500	> 500
Pd(0.5)Co(0.1)/BEA	-	-	456	549
Pd(0.5)Co(0.28)/BEA	-	-	379	496
Pd(0.5)Co(0.5)/BEA	-	-	357	473
Pd(0.5)Co(1.0)/BEA	488	0.826	352	420
Pd(0.5)Co(1.5)/BEA	-	-	360	430
Co(1.0)/BEA	428	0.782	> 500	> 500
Pd(1.0)/BEA	432	0.766	331	392

Table 2. Apparent activation energies of Pd(0.5)Co(x)/BEA (x = 0, 1.0), and Pd(1.0)/BEA catalysts.

Sample	Eapp (kJ/mol)
Pd(0.5)/BEA	46.3 ± 3.3
Pd(0.5)Co(1.0)/BEA	81.1 ± 5.1
Pd(1.0)/BEA	88.4 ± 5.4

Table 3. Relative energies of Co/BEA and Pd/BEA using both the PBE and BEEF-vdw functionals.

Structure	Relative energy (eV)	
	PBE	BEEF-vdw
Co/BEA	-2.02	-0.88
Pd/BEA	0.26	-0.58

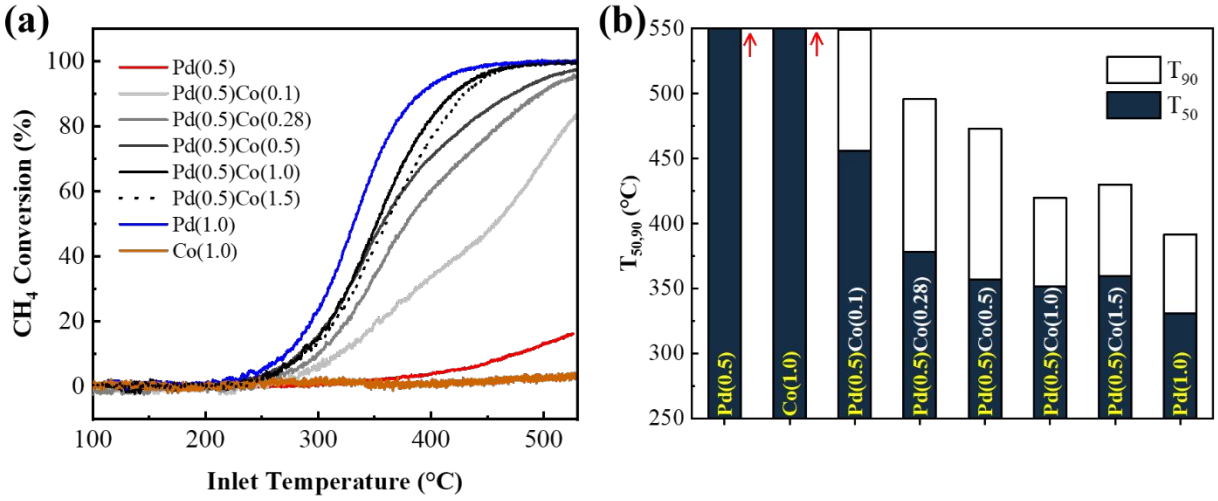

Fig. 1. (a) CH_4 oxidation light-off curves, and (b) $T_{50,90}$ of CH_4 oxidation over Pd(0.5)Co(x)/BEA (x = 0, 0.1, 0.28, 0.5, 1.0, 1.5), Co(1.0)/BEA, and Pd(1.0)/BEA catalysts.

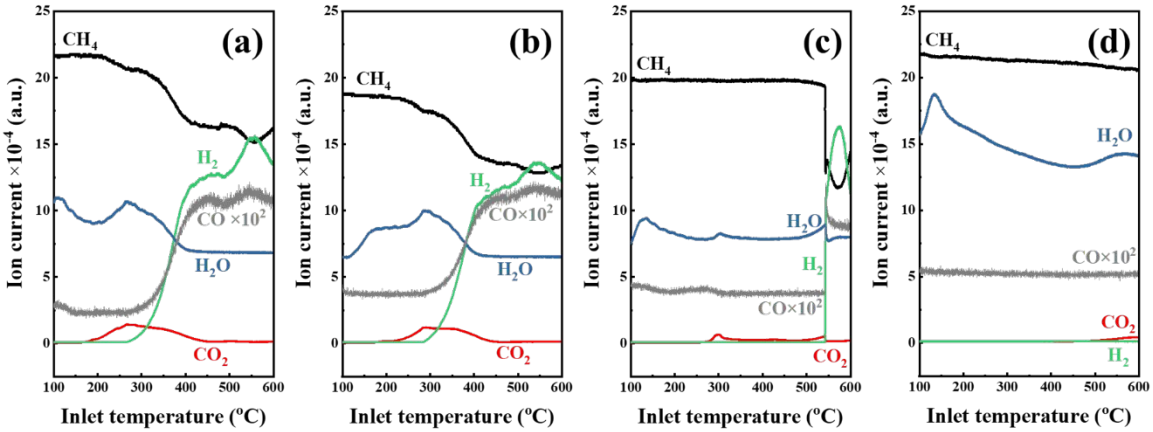

Fig. 2. CH_4-TPR over (a) Pd(1.0)/BEA, (b) Pd(0.5)Co(1.0)/BEA, (c) Pd(0.5)/BEA, and (d) Co(1.0)/BEA catalysts (1500 ppm CH_4, balanced by Ar (WHSV = 99,900 $mL g_{cat}^{-1} h^{-1}$)).

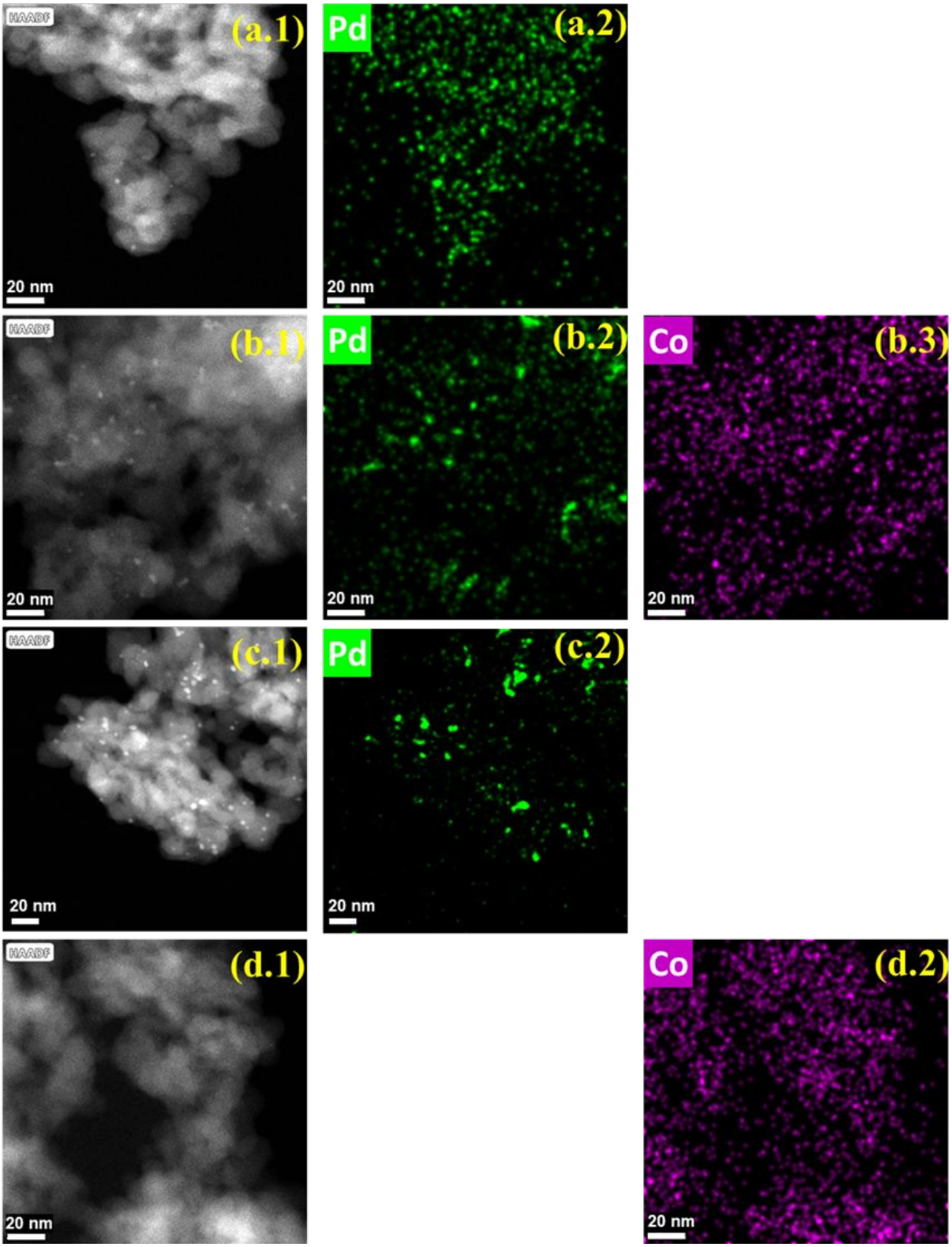

Fig. 3. HAADF-STEM images and EDS elemental (Pd, Co) maps of fresh (a.1, 2) Pd(0.5)/BEA, (b.1-3) Pd(0.5)Co(1.0)/BEA, (c.1, 2) Pd(1.0)/BEA, and (d.1, 2) Co(1.0)/BEA catalysts.

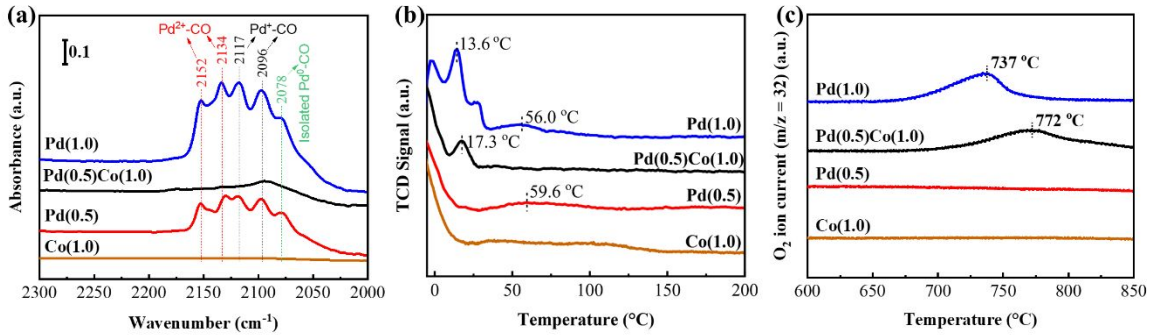

Fig. 4. (a) CO DRIFTS (b) H_2-TPR over fresh Pd(0.5)Co(x)/BEA (x = 0, 1.0), Pd(1.0)/BEA, and Co(1.0)/BEA catalysts, (c) O_2-TPD of used Pd(0.5)Co(x)/BEA (x = 0, 1.0), Pd(1.0)/BEA, and Co(1.0)/BEA catalysts.

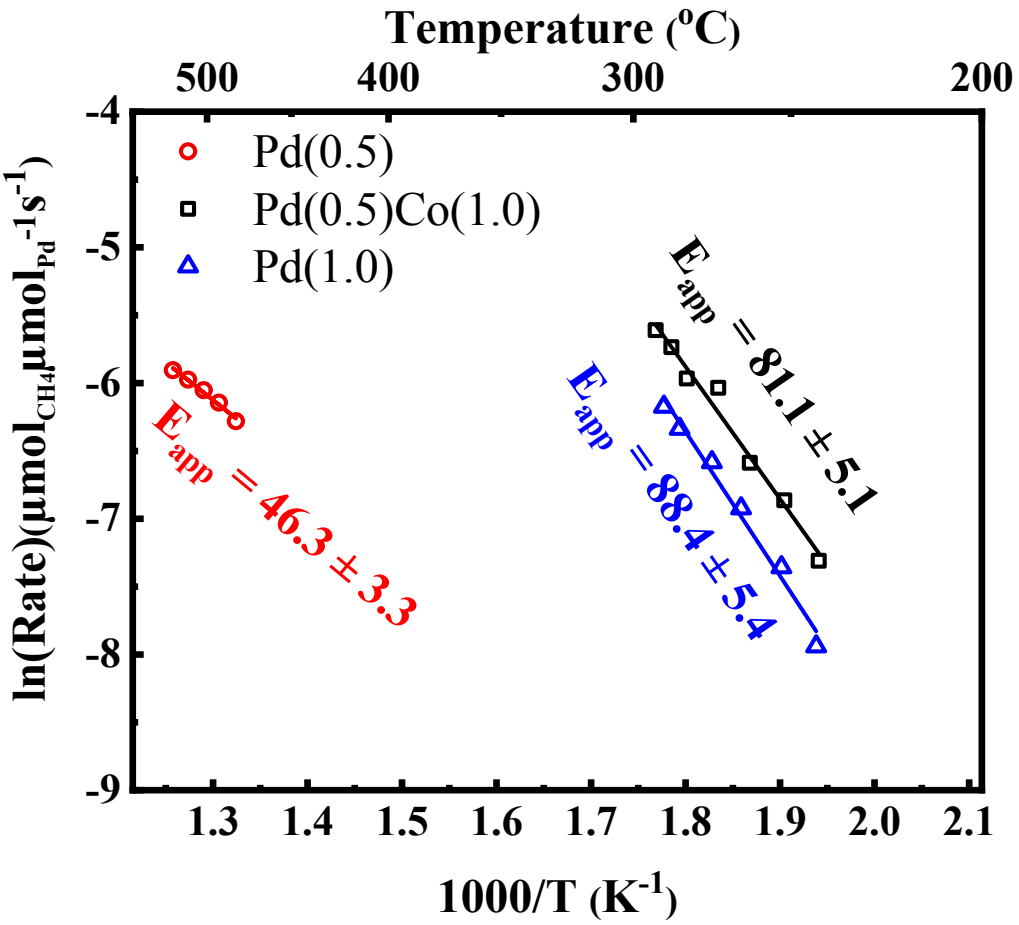

Fig. 5. Arrhenius plot and apparent activation energies for CH_4 oxidation over Pd(0.5)Co(x)/BEA (x = 0, 1.0) and Pd(1.0)/BEA catalysts.

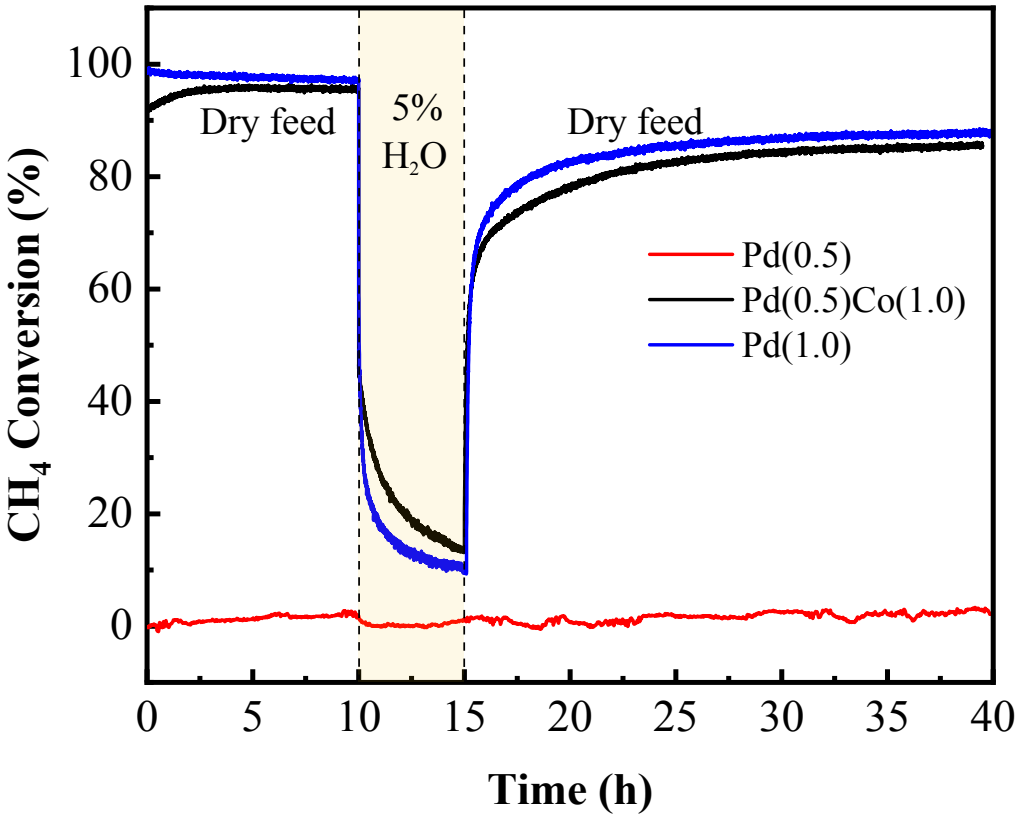

Fig. 6. Stability tests of CH_4 oxidation over Pd(0.5)Co(x)/BEA (x = 0, 1.0) and Pd(1.0)/BEA catalysts under dry (1500 ppm CH_4, 5% O_2, balanced by Ar) and wet (1500 ppm CH_4, 5% O_2, 5% H_2O, balanced by Ar) conditions, WHSV = 99,900 $mL g_{cat}^{-1} h^{-1}$.

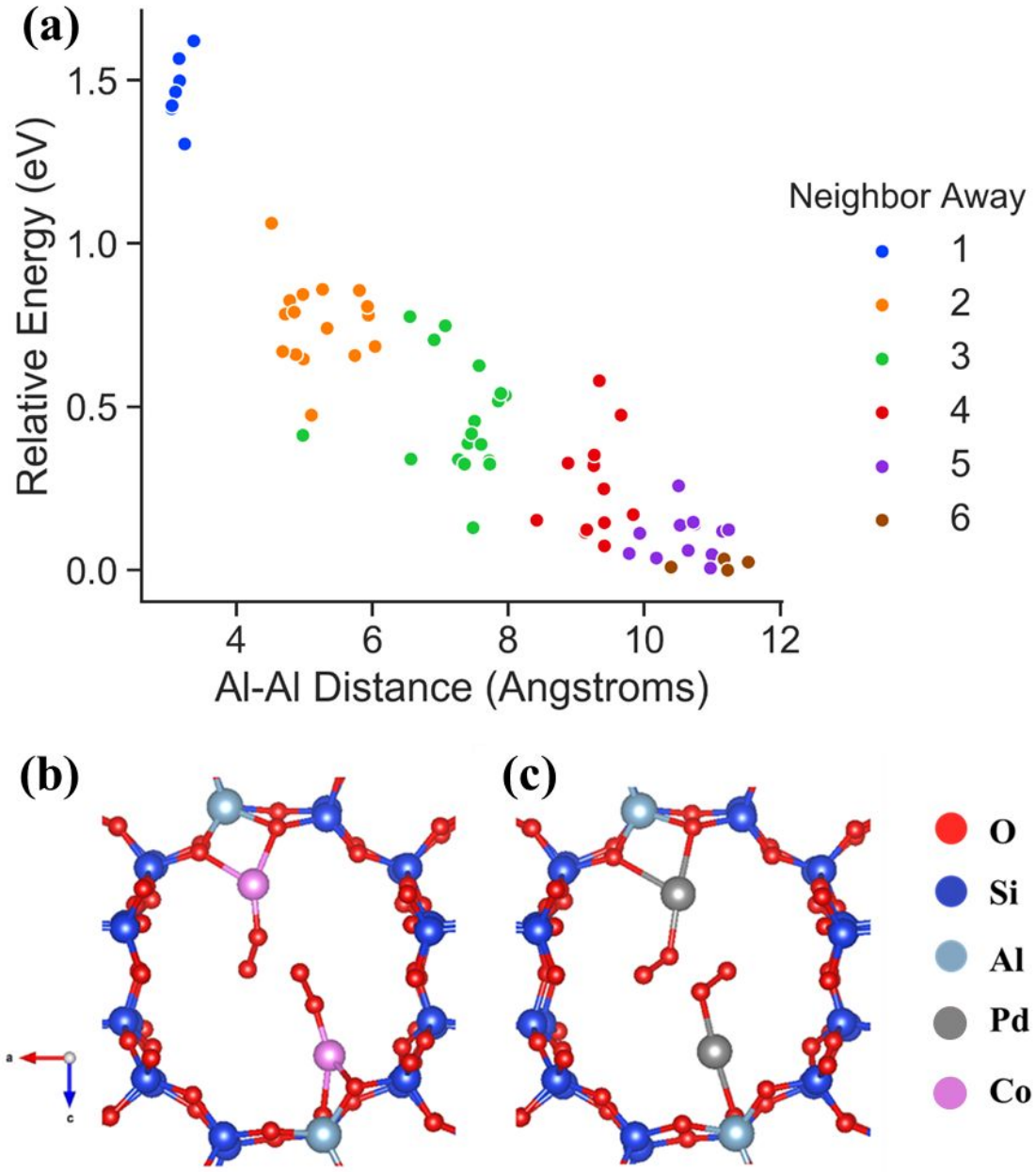

Fig. 7. (a) Relative energies of 70 different dual aluminum placements within a 12-membered ring channel in a single BEA unit cell calculated using the BEEF-vdw functional (Energies are taken relative to the lowest energy structure; Neighbor away refers to the number of T-sites between both aluminums). Final structures of (b) Co/BEA and (c) Pd/BEA. Geometries shown here are optimized using the BEEF-vdw functional.